2020

Potential of Module Arrangements to Enhance Convective Cooling in Solar Photovoltaic Arrays

B. Stanislawski
University of Utah

Fabien Margairaz
University of Utah

Raúl Bayoán Cal
Portland State University

Marc Calaf
University of Utah

Citation Details

Stanislawski, B., Margairaz, F., Cal, R. B., & Calaf, M. (2020). Potential of module arrangements to enhance convective cooling in solar photovoltaic arrays. Renewable Energy.

Renewable Energy 157 (2020) 851–858

Contents lists available at ScienceDirect

Renewable Energy

journal homepage: www.elsevier.com/locate/renene

Potential of module arrangements to enhance convective cooling in solar photovoltaic arrays

B. Stanislawski [a], F. Margairaz [a], R.B. Cal [b], M. Calaf [a, *]

[a] Department of Mechanical Engineering, University of Utah, 201 Presidents' Cir, Salt Lake City, UT, 84112, USA
[b] Department of Mechanical & Materials Engineering, Portland State University, 1825 SW Broadway, Portland, OR, 97201, USA

ARTICLE INFO

Article history:
Received 16 March 2020
Received in revised form
7 April 2020
Accepted 9 April 2020
Available online 17 April 2020

Keywords:
PV array arrangement
Surface thermal heterogeneity
Convective heat transfer
Control volume analysis
ABL-Solar farm interaction
Large-eddy simulation

ABSTRACT

When solar photovoltaic (PV) module temperatures rise during operation, commonly-installed modules experience an efficiency loss between 0.1 and 0.5% per degree above 25°C. Thus, extensive research has aimed to reduce the operating temperature of solar modules. However, many cooling solutions require additional cost or equipment that precludes their implementation in utility-scale PV plants. Based on previous studies of land-atmosphere interactions of surface thermal heterogeneity, we hypothesize that certain solar farm arrangements may enhance natural convective heat transfer between the solar modules and surrounding flow. Due to the strong non-linear relationship between module temperature and convective heat transfer, enhancing the convective cooling could have substantial impacts on module efficiency. Here, we investigate the potential impact of module arrangements on the convective cooling of large PV arrays. Three idealized module arrangements are evaluated in comparison to the traditional, row-organized arrangement. To characterize each arrangement, a non-dimensional packing parameter is developed. Numerical simulation results indicate that dense arrangements with larger packing parameters more effectively enhance convective cooling than sparse arrangements. Compared to the baseline, the most compact arrangement exhibited an increase in convective heat transfer of 14.8%. These results indicate that module arrangement plays an influential role in solar farm convective cooling.

1. Introduction

In its International Energy Outlook 2019, the U.S. Energy Information Administration predicted that renewable production would increase to 49% of the global electricity generation by 2050, with solar composing the fastest-growing share [1]. In alignment with the 2011 and 2016 SunShot Initiatives from the U.S. Department of Energy, the photovoltaic (PV) community aims to maximize solar module efficiency to further promote the adoption of solar energy. According to the Best Research-Cell Efficiency Chart proposed by the National Renewable Energy Laboratory (NREL), multi-crystalline PV technology, which constitutes 62% of total solar energy production at present [2], has reached 22.8% efficiency [3], and the average commercial wafer-based silicone module efficiency has reached 17% [2]. These efficiencies are determined in standard test conditions (STC: solar irradiance of 1000 W/m^2, air mass of 1.5, and cell temperature of 25°C); however, these conditions are rarely met in the field during solar farm operation. As operating temperatures rise above STC (25°C), the module efficiency drops. The efficiency of PV modules depends on several factors including solar cell material composition and operating temperature. Crystalline-silicon solar cells, which account for 95% of solar energy production [2], experience an efficiency loss between 0.1% and 0.5% per degree above STC (25°C) [4]. Solar modules in operation routinely exceed STC, reaching up to 70°C with average temperatures of 49°C in warm climates such as the U.S. southwest [4], which substantially curtails performance. Thus, extensive research has aimed to reduce the operating temperature of solar modules.

The relationship between module temperature and the local wind speed is characterized by the convective heat transfer coefficient h. As h increases, so does heat transfer from the warm solid surface to the cooler surrounding fluid through convection. In this way, the convective heat transfer coefficient is a measure of convective cooling. This strong relationship was first noted by

* Corresponding author.
E-mail address: marc.calaf@utah.edu (M. Calaf).

https://doi.org/10.1016/j.renene.2020.04.049

Griffith et al., in 1981, who illustrated that module temperature is highly sensitive to wind speed, less so to wind direction, and comparatively insensitive to ambient temperature [5]. Through assessments of methods for mitigating thermal losses, Vaillon et al. illustrated the strong non-linear relationship between the solar module operating temperature and h, highlighting that thermal convection plays a crucial role in module efficiency [6]. Consequently, they assert that future research should pursue the enhancement of conductive/convective heat transfer between solar modules and a cooler surrounding medium [6], which motivates this work.

Just as an urban canopy (i.e., city buildings) traps heat and diverts outside airflow around buildings, a large-scale solar farm affects the momentum and temperature of the local and mean flow. As a first step to understand these complex interactions, we focus solely on the thermal perturbations of the atmospheric flow by representing an idealized solar farm as flat, heated patches embedded in the ground surface. This simplification isolates the thermal impact of the solar farm from the pressure and wind speed variations induced by the physical topography of the solar modules. This idealized and canonical form of the problem is rooted in the interactions between surface thermal heterogeneity and the surrounding atmospheric flow. From an experimental approach, Jensen et al. studied near-surface heat flux of thermally heterogeneous surfaces and found that the variations in subsurface thermal characteristics drive the differing countergradient behavior [7]. From a numerical approach, Shao et al. developed a large-eddy simulation (LES) model that was applied to a heterogeneous surface and compared to measurements. They found a large variation of thermal fluxes due to large-eddy randomness, rapid large-eddy and surface feedback, and local advection related to surface heterogeneity [8]. To analyze the influence of idealized surface heterogeneity on virtual turbulent flux measurements, De Roo and Mauder conducted LES of surface temperature patches that varied in size and studied the advection and turbulent flux terms of the energy budget [9]. Kilometer-scale surface heterogeneity led to noticeable vertical updrafts and downdrafts, while hectometer-scale heterogeneity did not. Similarly, Margairaz et al. conducted LES of various length scales of heated surface patches and noted the long-lasting impact of the surface thermal heterogeneity on the mean flow through enhanced ventilation [10,11]. These findings bolster the hypothesis that the length scale and arrangement of surface thermal heterogeneity noticeably impact the surrounding atmospheric flow. While previous work has studied the land-atmosphere interactions, the PV community has not yet determined a mathematical relationship between the geometric characteristics of the heated patches (idealized solar modules in our case) and the enhancement of convective heat transfer. Our goal is to investigate the potential impact of solar farm arrangement on the enhancement of convective cooling under turbulent conditions, using numerical simulations of a simplified, idealized representation of solar farms. This work aims to shed light on the conductive/convective cooling strategy recommended by Vaillon et al. [6] to enhance plant-level PV efficiency.

To develop a relationship between the convective heat transfer coefficient h and the solar farm arrangement, four cases are studied using an LES framework and analyzed using a control volume approach. The manuscript is structured as follows. In section 2.1 and 2.2, we describe the LES framework and set-up used to generate the simulation data. In section 2.3, we derive the non-dimensional "packing parameter" used to characterize the arrangement of each case, and in section 2.4, we review the theory and analysis methods using the integrated enthalpy equation and control volume approach. Based on these methods, we illustrate the impact of various arrangements on the convective heat transfer coefficient as a measure of convective cooling in section 3. We then quantify the difference in the convective heat transfer coefficient among the four study cases, revealing that the compact arrangement, with the highest packing parameter, exhibits the highest h and thus, most effectively enhances convective cooling.

2. Methodology

2.1. Large-eddy simulation framework

Using an LES computational approach, the interaction between the atmospheric boundary layer and four cases of idealized solar farm arrangements is modeled. The framework is based on Albertson and Parlange [12,13], later modified by Bou-Zeid et al. [14], Calaf et al. [15], and Margairaz et al. [16]. A pseudo-spectral set-up is used to solve for the momentum $\tilde{u}_i$ ($i = 1, 2, 3$) and the potential temperature $\tilde{\theta}$, where the $\tilde{\cdot}$ denotes the LES-filtered variables. In this framework, the incompressible Navier-Stokes equations in rotational form are coupled with the temperature transport equation through the Boussinesq approximation. The time integration is carried out using a second-order Adam-Bashforth scheme [17]. The sub-grid models include the Lagrangian scale-dependent dynamic models for momentum and temperature [14,15]. The flow is driven by a mean pressure gradient imposing a horizontal geostrophic wind velocity ($U_g = 4\ m/s, V_g = 0\ m/s$) using the geostrophic approximation. A two-layer capping inversion is imposed at the top of the domain to prevent boundary layer growth following Sullivan and Patton [18].

This pseudo-spectral code computes the horizontal derivatives in Fourier space, which leads to periodic boundary conditions in the horizontal directions. Vertical derivatives are computed using second-order finite differences on a vertically staggered grid. Upper boundary conditions for the horizontal velocities are prescribed as stress-free ($\partial_z \tilde{u}_i = 0$, $i = 1, 2$) and a constant temperature gradient corresponding to the initial strength of the capping inversion ($\partial_z \tilde{\theta} = cst$). The non-penetration condition ($\tilde{w} = 0$) is imposed on the vertical velocity at the top and bottom of the domain. Lower boundary conditions for the horizontal velocities and temperature are specified using Monin-Obukhov similarity theory [19], which provides a formulation for the surface stress and surface heat flux corrected for atmospheric stability. Instantaneous surface stresses τ_{xz} and τ_{yz} are formulated as a function of the unit direction vector of the horizontal velocity [20,21] and friction velocity u_* at the first grid point ($\Delta z/2$). The friction velocity is given by

$$u_*^2 = \left[\frac{\kappa}{\ln\left(\frac{\Delta z/2}{z_0}\right) + \psi_m\left(\frac{\Delta z/2}{L}\right)}\right]^2 \left(\widehat{\tilde{u}}_1^2(x, y, \Delta z/2) + \widehat{\tilde{u}}_2^2(x, y, \Delta z/2)\right), \tag{1}$$

where the aerodynamic roughness length is denoted by z_0 and $\kappa = 0.4$ is the von Kármán constant. In Eq. (1), the velocity field $\tilde{u}_i$ is filtered a second time at $2\Delta_{LES}$, represented by $\widehat{\cdot}$, with $\Delta_{LES} = \sqrt{\Delta x \Delta y}$, which is the horizontal grid size. The stability correction function of momentum ψ_m is computed using Brutsaert's formulation [22] and depends on atmospheric stability, which is estimated by the local Obukhov length $L = -u_*^3 \theta_S / \kappa g q_s$, where θ_S is the surface temperature, g is the gravitational acceleration, and q_s denotes the kinematic surface heat flux [23].

Following the same procedure derived from Monin-Obukhov similarity theory, the vertical kinematic sensible heat flux is computed as

$$q_s = \frac{[\theta_s(x,y) - \tilde{\theta}(x,y,\Delta z/2)]}{\left[\ln\left(\frac{\Delta z/2}{z_{0s}}\right) + \psi_s\left(\frac{\Delta z/2}{L}\right)\right]}\kappa u_*, \quad (2)$$

where ψ_s is the stability correction function for the temperature and z_{0s} is the aerodynamic roughness length of heat, which is set to $0.1z_0$ as commonly accepted in literature [23]. Although this framework was developed for idealized homogeneous surfaces, this approach provides acceptable results in the case of non-homogeneous conditions [20,24–26].

2.2. Large-eddy simulation set-up

In the LES framework, an idealized solar farm is represented as a set of heated patches embedded in the ground surface. Four study cases of solar farm arrangements are depicted in Fig. 1. To clarify nomenclature, each black "patch" shown in Fig. 1 represents a set of adjacent solar modules. Highlighted in Table 2, the four cases represent varied layout and grouping, or packing, of the solar modules subjected to a mean geostrophic wind forcing of 4 m/s. The baseline case reflects the traditional row-organized arrangement of solar modules within utility-scale solar arrays. To study the impact of module grouping and row-spacing, the scattered, distant, and compact cases are designed to vary both the patch size and the density of patches within the solar farm. In all four cases, the same amount of thermal energy is supplied through the solar and ground surfaces. Namely, the total surface area of solar patches A_p occupies 6% of the total domain surface area, with a minimal 7% percent difference with respect to the baseline case.

Table 1 details the LES parameters used for all four simulations. Based on experimental data collected at NREL, the solar module and ground surface temperatures increase gradually over 4 h, reaching daytime values found in Table 1. The temporal resolution is selected to ensure the stability of the time integration. Table 2 describes the physical parameters of each study case, in which N_m represents the number of solar modules, p_x and p_y represent the x- and y-dimensions of a solar module patch, respectively, s_x and s_y represent the x- and y-dimensions of the spacing between modules, and x_{CV} and y_{CV} represent the x- and y-dimensions of the control volumes used for analysis, as illustrated in Fig. 2. The height of the control volumes used for analysis is set at $z/z_i = 0.28$, which is near enough to the ground surface to capture surface temperature effects, yet far enough away to damp out noise from temperature discontinuities at the surface associated with the law of the wall.

2.3. Non-dimensional scaling of convective cooling in solar farms

In order to characterize the four cases based on arrangement and thermal variations, a non-dimensional packing parameter φ of the solar farm is introduced. Based on terminology from gerrymandering strategies in the field of political science [27], we classify more dense module arrangements as "packed" and more sparse arrangements as "cracked." Inspired by the thermal heterogeneity parameter $\mathscr{H}$ in Ref. [11], the proposed thermal packing parameter depends on both the size of the solar patch and the grouping of these patches within a certain area. For example, if all solar modules were packed together into one massive set with no spacing among modules, the associated φ value would equal 21.2, a comparatively large φ value. However, if this large mass of solar modules was then separated, or cracked, into a sparse arrangement of individual modules with significantly large spacing, the φ value would approach zero. This non-dimensional packing parameter is defined as

$$\varphi = \frac{gL_{sf}}{U_G^2}\frac{\Delta\overline{\theta_s}}{\overline{\theta_s}}, \quad (3)$$

where g refers to gravitational acceleration, U_G refers to the mean geostrophic wind speed, and L_{sf}, the dimensional solar farm length scale with units of meters is defined as

$$L_{sf} = p \cdot P_{AF}^2. \quad (4)$$

Here, the solar module patch scale is defined as $p = \sqrt{p_x p_y}$ (see Fig. 2) and P_{AF} is the plan area fraction defined as $P_{AF} = A_p/A_{sf}$. A_p denotes the total surface area of the solar module patches and A_{sf} denotes the surface area of the solar farm, which is defined as the area inside the perimeter delineated by the outermost edges of the solar patches. This solar farm length scale L_{sf} captures the contributions from the size of the solar module patch and from the packing of the patches within the solar farm area. The second factor in the solar farm packing parameter, $\Delta\overline{\theta_s}/\theta_s$, represents the normalized mean absolute difference between the surface temperature at a point and the averaged surface temperature, $\Delta\theta_s = \langle|\overline{\theta_s} - \langle\overline{\theta_s}\rangle|\rangle$, within the control volume.

The solar farm packing parameter is developed to reflect the tendency of the arrangement to induce a buoyancy-driven plume. To illustrate the plume effect, imagine that a 2×2 array of solar

Table 1
Large-eddy simulation parameters.

Quantity	Symbol	Units	Value
Domain size	L_x, L_y, L_z	km	$2\pi, 2\pi, 2$
Number of gridpoints	N_x, N_y, N_z	(−)	128, 128, 256
Spatial resolution	$\Delta x, \Delta y, \Delta z$	m	49.1, 49.1, 7.8
Temporal resolution	Δt	s	0.05
Spin-up time	(−)	s	16,200
Data capture time	(−)	s	7200
Module temperature	θ_m	K	333
Ground temperature	θ_g	K	313

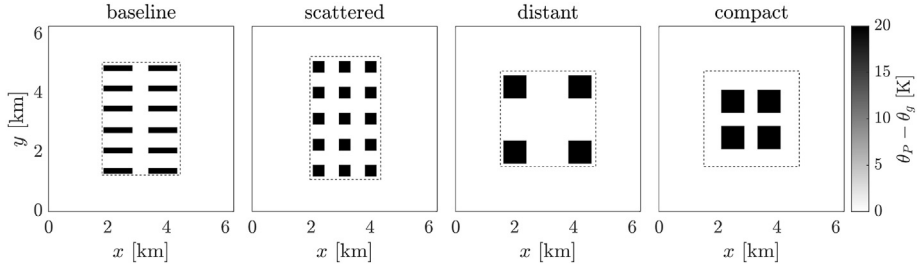

Fig. 1. Top view of four study cases of idealized solar farm arrangements. Dark areas represent the heated patches and the dashed line represents the perimeter of the control volume for each case.

Table 2
Geometric parameters of the four study cases. Geometric variables are depicted in Fig. 2

	Case	$\varphi[-]$	$N_{mx}*N_{my} = N_m$	$p_x, p_y[m]$	$s_x, s_y[m]$	$x_{CV}, y_{CV}[km]$
0	baseline	0.38	2*6 = 12	982, 196	540, 491	2.70, 3.88
1	scattered	0.39	3*5 = 15	393, 393	491, 491	2.45, 4.22
2	distant	0.80	2*2 = 4	785, 785	1,424, 1424	3.29, 3.29
3	compact	3.9	2*2 = 4	785, 785	442, 442	3.29, 3.29

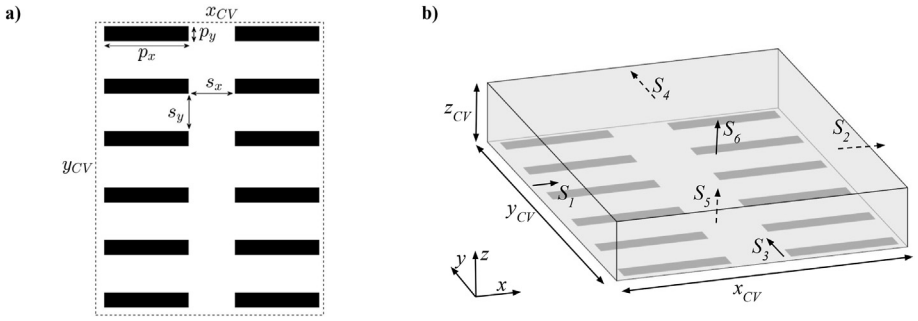

Fig. 2. a) Schematic of geometric dimensions used to describe the four study cases in Table 2; b) Control volume approach used in the analysis.

patches were four separate bonfires sparsely distributed over a large field. Then imagine those four bonfires placed adjacent to one another in the center of the field. The latter case will generate a larger, more powerful smoke plume than the sparsely-distributed fires. Subsequently, the latter case will have a higher value of φ because of the high degree of packing. In the context of the four study cases presented, the baseline case has the smallest value of φ because the solar patches are the most cracked, or sparse. This case has a smaller value of φ than the scattered case because of the arrangement of modules in rectangular rows instead of in square sets, limiting the plume effect. On the contrary, the compact case corresponds to the highest value of φ because of both the grouping of modules into large patches and the dense packing of these patches.

2.4. Analysis of large-eddy simulation results

To assess the heat transfer variations induced by each idealized solar farm case, we apply a control volume approach similar to that described by DeRoo and Mauder [9] and Cortina et al. [28]. Starting from the theory underlying the analysis, the enthalpy equation is introduced as

$$\rho C_p \frac{\partial \overline{\theta}}{\partial t} + \rho C_p \overline{u}_j \frac{\partial \overline{\theta}}{\partial x_j} = -\rho C_p \frac{\partial \left(\overline{u_j' \theta'}\right)}{\partial x_j} + S, \tag{5}$$

where ρ is the air density, C_p is the specific heat of the air at constant pressure, $\overline{\theta}$ is the time-averaged air temperature, t is time, $\overline{u}_j$ is the time-averaged wind velocity in the j direction, and x_j refers to distance in the j cardinal directions, x, y, z. The overbar denotes time-averaged variables and the prime denotes turbulent fluctuations from the time-averaged value. The first three terms represent storage, advection, and turbulent flux divergence, respectively, and S represents the heat source from the surface into the atmosphere. Integration of Eq. (5) over the pre-defined control volume around the solar farm yields

$$\underbrace{\rho C_p \int_{CV} \frac{\partial \overline{\theta}}{\partial t} dV}_{Q_{st}} + \underbrace{\rho C_p \int_{CV} \frac{\partial \left[\overline{u}_j \left(\overline{\theta} - \theta_{ref}\right)\right]}{\partial x_j} dV}_{Q_{adv}} + \underbrace{\rho C_p \int_{CV} \frac{\partial \left(u_j' \theta'\right)}{\partial x_j} dV}_{Q_{turb}} = \underbrace{\int_{CV} S dV}_{Q_s}, \tag{6}$$

where Q_{st} denotes the storage heat rate, Q_{adv} the advection heat rate, Q_{turb} the turbulent heat rate, and Q_s the source heat rate. The source term is expanded into two components, where $Q_s = Q_{sf} + Q_g$, or solar farm heat rate plus ground heat rate. The ground heat rate can be rewritten as $\langle q_g \rangle A_g$ where $\langle q_g \rangle$ is the spatially-averaged ground heat flux and A_g represents the area of the ground, not including the solar modules. Here, Q represents heat rate $[W]$ and q represents heat flux $[W/m^2]$. In these equations, the $\tilde{\cdot}$ to denote LES-filtered variables has been omitted for convenience. Neglecting storage because it is small and expanding the source term, Eq. (6) is rewritten in simpler terms,

$$Q_{sf} = Q_{adv} + Q_{turb} - \langle q_g \rangle A_g. \tag{7}$$

Based on this derivation, the equations used for the analysis are developed. After applying Gauss's theorem to convert the volume integrals into surface integrals and separating horizontal terms from vertical terms, the following equation is obtained and used to compute Q_{sf}, the solar farm heat rate

$$Q_{sf} = \rho\, C_p \sum_{k=1}^{4} \int_{S_k} \left[\overline{\mathbf{u}}_{\perp} \left(\overline{\theta} - \theta_{ref}\right)\right] dS_k + \rho\, C_p \int_{S_6} \left[\overline{w} \left(\overline{\theta} - \theta_{ref}\right) \times\right] dS_6 + \rho\, C_p \sum_{k=1}^{4} \int_{S_k} \left(\overline{\mathbf{u}'_{\perp} \theta'}\right) dS_k + \rho\, C_p \int_{S_6} \left(\overline{w'\theta'}\right) dS_6 - \langle q_g \rangle A_g. \tag{8}$$

Here, S_k refers to the surface of the numbered lateral faces of the control volume as depicted in Fig. 2, $\mathbf{u}_{\perp}$ is the wind velocity perpendicular to the lateral control volume faces, w is the wind velocity in the vertical direction, S_6 is the top face of the control volume, and θ_{ref} is the reference temperature taken as θ_{∞}.

Eq. (8) indicates that the heat rate into the control volume from

the ground (from both solar patches and ground cover) is equal to the net advective and turbulent heat rates exiting the control volume. This approach is depicted in Fig. 2. The control volume sizes were determined to minimize the x- and y-dimensions, while maintaining an identical (within 4%) ratio of solar patch area to ground cover area across all cases.

Once Q_{sf} is calculated, this value is used as an input in Newton's Law of Cooling to compute the overall solar farm convective heat transfer coefficient, h, associated with each arrangement:

$$h = \frac{Q_{sf}}{A_p(\theta_p - \theta_\infty)}. \tag{9}$$

Here, A_p denotes the total area of the solar module patches, θ_p denotes the temperature of the solar module surface, and θ_∞ is taken at $z/z_i = 0.5$ as the unperturbed ambient temperature. In the next section, results from Eq. (8) and Eq. (9) are presented.

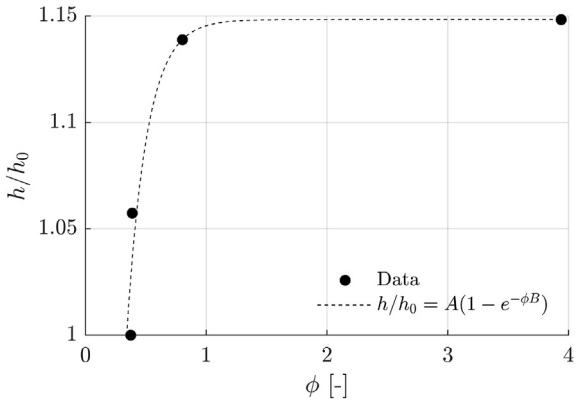

Fig. 4. The convective heat transfer coefficient h as a function of the packing parameter φ. Data from the four study cases are shown in filled circles with normalized values of h/h_0, where h_0 refers to h the baseline case. The dashed line represents an exponential fit of the form $h/h_0 = A(1 - e^{-\varphi B})$.

3. Results

To illustrate the impact of the idealized solar farms on the surrounding flow, results from the LES of the four study cases are presented in Fig. 3. These iso-surface visualizations illustrate the impact of the solar farm on the mean vertical velocity and the temperature field of the surrounding flow. The larger patch sizes in both the distant and compact cases create noticeable buoyancy-induced plumes, driven by increased upward vertical velocity. In the distant case, four distinct plumes of upward vertical velocity are illustrated above the four larger patches, each exhibiting heated air stretching upward into the atmosphere. However, in the compact case, the plumes of upward vertical velocity are less distinct and instead have combined into a single, but less distinct, larger plume. The high-temperature air above the patches reaches highest in the distant case, but the large plume of upward velocity appears to dominate in the compact case. The smaller solar patches in the baseline and scattered cases tend to generate less distinct plumes than in the latter cases. Due to the blending of these plumes in the surrounding flow, the heat from the smaller solar patches does not reach as far into the atmosphere. These results indicate that the larger solar module patches have a more prominent impact on the mean atmospheric flow through an enhanced plume effect.

To quantify the convective cooling of each arrangement, we compute the convective heat transfer coefficient h as a function of the packing parameter φ using the methods in section 2.4. As highlighted in Fig. 4, there exists an exponential relationship whereby, as φ increases and arrangements become more closely packed, the convective cooling, represented by h, also increases.

The baseline case corresponds to the smallest values of φ and h whereas the compact case exhibits the largest values. With a value of φ approximately 10 times larger than that of the baseline case, the compact case demonstrates a 14.8% increase in h over the

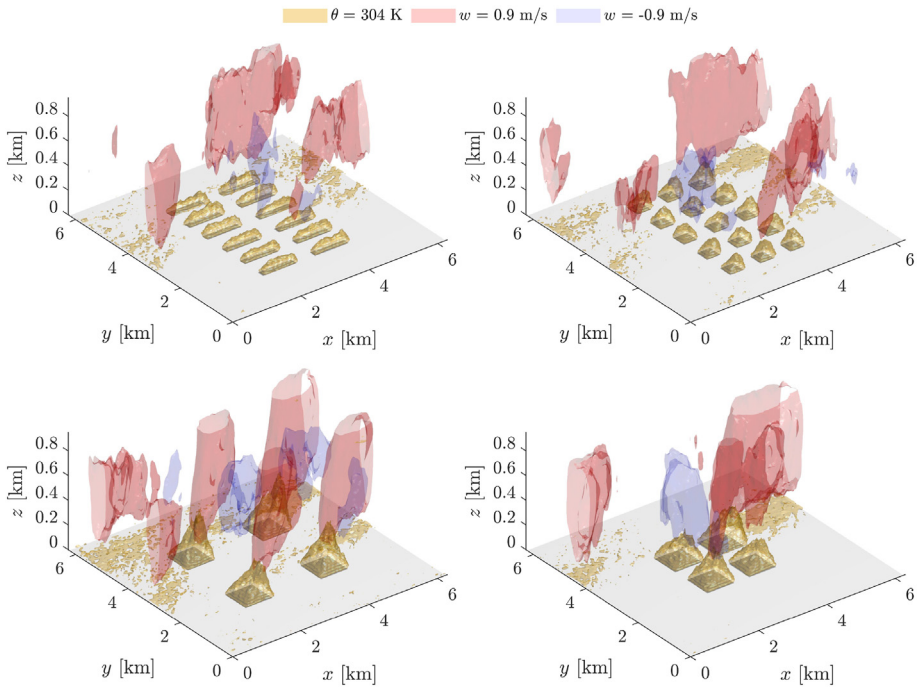

Fig. 3. Iso-surfaces of the mean vertical velocity $\overline{w}$ and temperature $\overline{\theta}$ for all four cases. Red and blue iso-surfaces denote upward and downward vertical velocity, respectively, while yellow iso-surfaces denote high-temperature air above the solar module patches.

baseline. To determine the relationship between φ and h, the exponential curve, represented by the dashed line in Fig. 4, was fitted of the form $h/h_0 = A(1 - e^{-\varphi B})$, where $A = h_{max}/h_0$, and $B = 6$. This fit results in a root-mean-square error (RMSE) of 1.125%. However, more data points are needed to test this exponential law. The limit of this model, as φ approaches 0, yields an h/h_0 approaching 0 as well. The physical implication of φ approaching 0 refers to a case in which the size of the solar patch becomes infinitesimally small and the spacing between patches becomes infinitely large. In this case, the heat source that generates the buoyancy-driven plumes becomes negligible, resulting in negligible convective heat transfer.

To understand these differences in the convective heat transfer coefficient and the underlying physical processes, we evaluate the magnitude of each contributing term in the integrated enthalpy equation over the control volume (Eq. (7)). These results can be found in Fig. 5. Dominated by the turbulent heat rate, the results show that the compact case, with the highest value of φ, also exhibits the highest turbulent heat rate, while the distant case exhibits the lowest turbulent heat rate. Contrarily, the distant case, with $\varphi = 0.80$, shows the highest advective heat rate. Although there is no clear trend within each term, we observe an inverse relationship between the advective and turbulent heat rate terms. Because the ground heat rate remains relatively constant among the cases, the balance in net energy rate out of the control volume must be achieved by the advective and turbulent terms. As more energy leaves the control volume through the turbulent heat rate, less energy remains to exit through the advective heat rate. In Fig. 5b, we see the same trend as in Fig. 4, an exponential increase of Q_{sf} as a function of φ. When φ equals 3.9 in the compact case, Q_{sf} exhibits a 22.5% increase in solar farm heat rate as compared to the baseline case, leading to the strongest convective cooling.

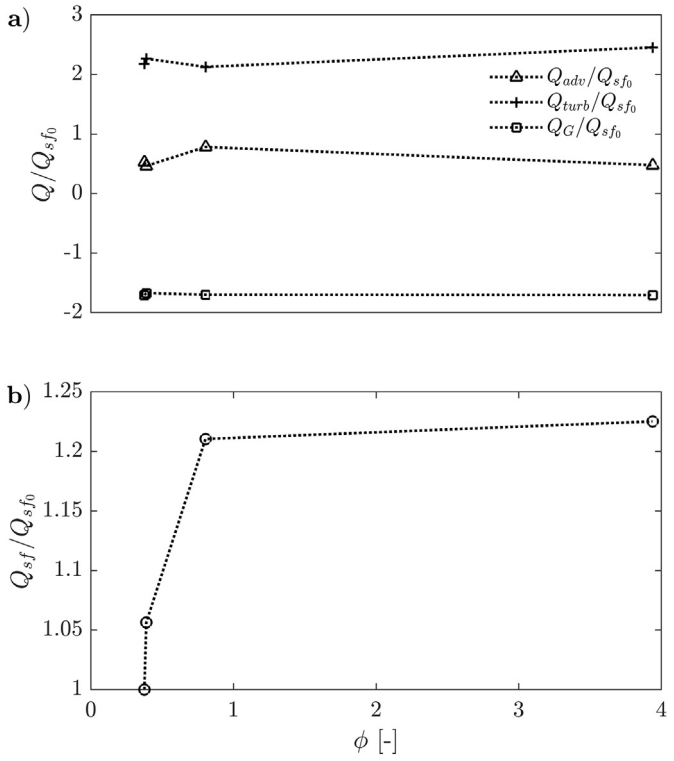

Fig. 5. Advective, turbulent, ground, and total solar farm heat rate terms of the integrated enthalpy equation. All terms are normalized by Q_{sf_0}, the total solar farm heat rate of the baseline case.

To further understand the underlying reasons for these differences, we examine the magnitude of each term at each face of the control volume as computed in Eq. (8) (see Fig. 6). While the total advective heat rate is smaller in magnitude than the total turbulent heat rate, we see comparatively higher magnitudes of advective heat rate in the streamwise and spanwise directions represented by S_1 through S_4. The advective heat rate of the baseline case, with the smallest φ, dominates in the x-direction, and the distant case more than doubles the y-direction magnitude of the other cases. In the vertical direction, the two cases with the highest φ have the highest advective heat rates, approximately tripling the magnitude of the baseline case. The turbulent heat rates exhibit negligible contribution from the horizontal directions. In the vertical direction, both the scattered and compact cases exhibit comparatively high turbulent heat rates. The compact case, with the highest φ value, exhibits the highest turbulent heat rate, exceeding that of the baseline case by 6.7%. Since the exponential trend seen in h versus φ is not observed in either of these terms on its own, it is the combined effect of both contributing terms that leads to the positive relationship between the packing parameter and convective cooling. In the vertical direction, the large magnitudes of the advective and turbulent heat rates induced by both the distant and compact cases signify the impact of those arrangements on both the mean and instantaneous vertical motions and thermal variations. However, the baseline arrangement is associated with both the minimum advective and turbulent heat rates in the vertical direction, indicating a smaller momentum and thermal impact on the mean and instantaneous flow. This detailed investigation into the individual terms of the enthalpy equation improves our understanding of the relationship between the packing parameter and the convective heat transfer coefficient.

4. Discussion

If solar farm arrangements were unimportant, the figures presented in section 3 would show minimal differences among the results of all cases, but this is not the case. The 14.8% difference between the convective heat transfer coefficients of the baseline and compact cases illustrates the substantial impact of solar farm arrangement on heat transfer from an idealized solar farm to the

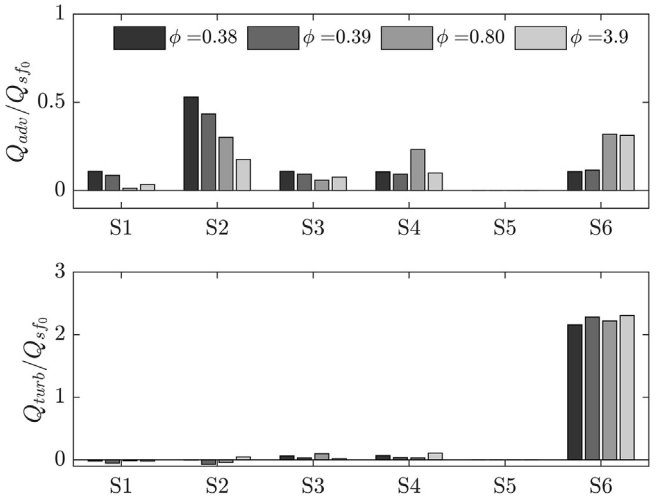

Fig. 6. Magnitude of the advective heat rate (upper) and turbulent heat rate (lower) at each face of the control volume. The total heat rate for each term is computed as $S_2 - S_1 + S_4 - S_3 + S_6 - S_5$. All terms are normalized by Q_{sf_0}, the total solar farm heat rate of the baseline case. Please note that the axis in Fig. a) reaches 1, whereas the axis in Fig. b) reaches 3.

atmosphere. Although the same amount of thermal energy is supplied to all cases, the heat is extracted from the modules and transferred throughout the domain differently in each case. Remarkably, the findings show that the more packed, less cracked, arrangements correspond to higher values of the convective heat transfer coefficient h of the solar farm. In other words, idealized solar farm arrangements that pack solar modules in close proximity lead to a higher packing parameter φ and increased convective cooling. We hypothesize that the larger patch size and denser packing create a compounded plume effect. This hypothesis is supported by the strong advective and turbulent heat rates in the vertical direction that correspond with the higher packing parameter. The results illustrate a trend in which higher values of φ create larger coherent structures in the flow that transfer heat away from the ground surface. This trend is also observed by Margairaz et al., who found that higher values of the thermal heterogeneity parameter ($\mathscr{H} > 5$) indicated that surface thermal heterogeneity strongly impacted the mean flow [11]. With four large heated patches of equal size, the distant and compact cases only differ in horizontal spacing. This difference manifests in the increased φ and h values in the compact case. By reducing the inter-row spacing between the four patches, the compact case aggregates the coherent structures above the individual patches into a compounded, stronger plume. Among the four idealized cases, the compact case most effectively transfers heat from the solar farm to the atmospheric flow and thus most effectively enhances convective cooling.

Results indicate that modifying the arrangement of solar modules is a viable method for decreasing module temperatures and thus should be further investigated. However, these findings result from highly canonical conditions and therefore should not be directly applied to the development of improved design standards for solar farms. These simulations reflect the case of weak mean wind speeds, where convective cooling is driven by the presence of large patches of surface thermal heterogeneity. However, in the presence of higher mean wind speeds, it is possible that smaller patches with increased spacing could enhance convective cooling. To inform future solar farm design practices, the cooling effects of solar farm arrangements under additional atmospheric conditions should be assessed.

As a first step, the results presented herein indicate that solar farm arrangement has the potential to significantly impact plant-level efficiency. The simplified power output model of Vaillon et al. [6] was used to compute the approximate impact of this increase in h on the power output. Based on this model, a 14.8% in h could yield an 8.4% increase in power output at lower h values (from 10 to 11.5 W/m^2K). However, for higher h values above 65 W/m^2K, the power output increase could reduce to a negligible value of 0.73%. Because this study considers simplified, idealized surface patches instead of three-dimensional solar modules, the exact values of h are not computed and only normalized values are presented. The substantial differences in h among the study cases highlight a potential impact of solar farm arrangement and suggest that further development and validation is needed to apply these findings to realistic solar farms.

5. Conclusions

In this work, a canonical first-order approximation analysis is conducted to determine the potential impact of solar farm arrangements on the enhancement of convective cooling. To characterize the arrangement of each solar farm, a non-dimensional packing parameter φ is developed. Sparse, or cracked, arrangements have small values of φ, whereas dense, or packed, arrangements have large values of φ. The results of four idealized study cases indicate that packing idealized solar modules in close proximity, which increases φ, can exponentially increase convective heat transfer of the solar farm. Both the advective and turbulent heat rates contribute to this trend, which reflects the tendency of larger solar patches and smaller inter-row spacing to impact the atmospheric flow through an enhanced plume effect. Future work should expand upon this analysis by considering the momentum impact of realistic solar farm topography in addition to the thermal impact. The simplified approach in this study provides a pathway to further investigate solar farm arrangement as a strategy for reducing module operating temperature and increasing plant-level efficiency.

Declaration of competing interest

The authors declare that they have no known competing financial interests or personal relationships that could have appeared to influence the work reported in this paper.

CRediT authorship contribution statement

B. Stanislawski: Methodology, Formal analysis, Investigation, Visualization, Writing - original draft. **F. Margairaz:** Methodology, Software, Data curation, Visualization. **R.B. Cal:** Supervision, Writing - review & editing. **M. Calaf:** Conceptualization, Supervision, Resources, Writing - review & editing.

Acknowledgements

This work is partially supported by the U.S. Department of Energy [grant number DE-EE0008168]. Dr. Calaf also acknowledges the Mechanical Engineering Department at the University of Utah for start-up funds and the Center for High Performance Computing (CHPC) at the University of Utah for computing resources.

References

[1] U.S. Energy Information Administration, International Energy Outlook (2019).
[2] Fraunhofer institute for solar energy systems, ISE, PHOTOVOLTAICS REPORT, URL: https://www.ise.fraunhofer.de/content/dam/ise/de/documents/publications/studies/Photovoltaics-Report.pdf, 2019.
[3] National Renewable Energy Laboratory (NREL), Best research-cell efficiency Chart, URL: https://www.nrel.gov/pv/assets/pdfs/best-research-cell-efficiencies.20191106.pdf, 2019. (Accessed 22 January 2020).
[4] O. Dupré, R. Vaillon, M.A. Green, Thermal Behavior of Photovoltaic Devices: Physics and Engineering, Springer, 2017.
[5] J.S. Griffith, M.S. Rathod, J. Paslaski, Some tests of flat plate photovoltaic module cell temperatures in simulated field conditions, in: 15th Photovoltaic Specialists Conference, 1981, pp. 822–830. URL: http://adsabs.harvard.edu/abs/1981pvsp.conf..822G.
[6] R. Vaillon, O. Dupré, R.B. Cal, M. Calaf, Pathways for mitigating thermal losses in solar photovoltaics, Sci. Rep. 8 (2018) 1, https://doi.org/10.1038/s41598-018-31257-0.
[7] D.D. Jensen, D.F. Nadeau, S.W. Hoch, E.R. Pardyjak, Observations of near-surface heat-flux and temperature profiles through the early evening transition over contrasting surfaces, Boundary-Layer Meteorol. 159 (2016) 567–587, https://doi.org/10.1007/s10546-015-0067-z.
[8] Y. Shao, S. Liu, J.H. Schween, S. Crewell, Large-eddy atmosphere-land-surface modelling over heterogeneous surfaces: model development and comparison with measurements, Boundary-Layer Meteorol. 148 (2013) 333–356, https://doi.org/10.1007/s10546-013-9823-0.
[9] F. De Roo, M. Mauder, The influence of idealized surface heterogeneity on virtual turbulent flux measurements, Atmos. Chem. Phys. 18 (2018) 5059–5074, https://doi.org/10.5194/acp-18-5059-2018. URL: https://www.atmos-chem-phys.net/18/5059/2018/.
[10] F. Margairaz, E. Pardyjak, M. Calaf, Surface Thermal Heterogeneities and the Atmospheric Boundary Layer: the Relevance of Dispersive Fluxes, Boundary-Layer Meteorology, ACCEPTED FOR PUBLICATION, 2020a.
[11] F. Margairaz, E. Pardyjak, M. Calaf, Surface Thermal Heterogeneities and the Atmospheric Boundary Layer: the Thermal Heterogeneity Parameter, Boundary-Layer Meteorology, ACCEPTED FOR PUBLICATION, 2020b.
[12] J.D. Albertson, M.B. Parlange, Surface length scales and shear stress: implications for land-atmospheric interaction over complex terrain, Water Resour.

Res. 35 (1999a) 2121–2132.
[13] J.D. Albertson, M.B. Parlange, Natural integration of scalar fluxes from complex terrain, Adv. Water Resour. 23 (1999b) 239–252, https://doi.org/10.1016/S0309-1708(99)00011-1.
[14] E. Bou-Zeid, C. Meneveau, M. Parlange, A scale-dependent Lagrangian dynamic model for large eddy simulation of complex turbulent flows, Phys. Fluids 17 (2005), 025105. http://scitation.aip.org/content/aip/journal/pof2/17/2/10.1063/1.1839152. http://aip.scitation.org/doi/10.1063/1.1839152, 10.1063/1.1839152.
[15] M. Calaf, M.B. Parlange, C. Meneveau, Large eddy simulation study of scalar transport in fully developed wind-turbine array boundary layers, Phys. Fluids 23 (2011) 126603. URL: http://scitation.aip.org/content/aip/journal/pof2/23/12/10.1063/1.3663376, 10.1063/1.3663376.
[16] F. Margairaz, M.G. Giometto, M.B. Parlange, M. Calaf, Comparison of dealiasing schemes in large-eddy simulation of neutrally stratified atmospheric flows, Geosci. Model Dev. (GMD) 11 (2018) 4069–4084, https://doi.org/10.5194/gmd-11-4069-2018. https://www.geosci-model-dev-discuss.net/gmd-2017-272/. https://www.geosci-model-dev.net/11/4069/2018/.
[17] J. Canuto, V.M. Goldman, I. Chasnoc, Turbulent viscosity, Astron. Astrophys. 200 (1988) 291–300.
[18] P.P. Sullivan, E.G. Patton, The effect of mesh resolution on convective boundary layer statistics and structures generated by large-eddy simulation, J. Atmos. Sci. 68 (2011) 2395–2415, https://doi.org/10.1175/JAS-D-10-05010.1.
[19] A. Monin, a.M. Obukhov, Basic laws of turbulent mixing in the surface layer of the atmosphere, Contrib. Geophys. Inst. Acad. Sci. USSR 24 (1954) 163–187.
[20] E. Bou-Zeid, C. Meneveau, M.B. Parlange, Large-eddy simulation of neutral atmospheric boundary layer flow over heterogeneous surfaces: blending height and effective surface roughness, Water Resour. Res. 40 (2004) n/a–n/a. URL: http://onlinelibrary.wiley.com/doi/10.1029/2003WR002475/full, 10.1029/2003WR002475.
[21] M. Hultmark, M. Calaf, M.B. Parlange, A new wall shear stress model for atmospheric boundary layer simulations, J. Atmos. Sci. 70 (2013) 3460–3470. URL: http://journals.ametsoc.org/doi/abs/10.1175/JAS-D-12-0257.1. doi:10.1175/JAS-D-12-0257.1.
[22] W. Brutsaert, Hydrology, Cambridge University Press, Cambridge, 2005. URL: http://ebooks.cambridge.org/ref/id/CBO9780511808470, 10.1017/CBO9780511808470.
[23] W. Brutsaert, Evaporation into the Atmosphere, Springer Netherlands, Dordrecht, 1982. URL: http://link.springer.com/10.1007/978-94-017-1497-6, 10.1007/978-94-017-1497-6.
[24] R. Stoll, F. Porté-Agel, Dynamic subgrid-scale models for momentum and scalar fluxes in large-eddy simulations of neutrally stratified atmospheric boundary layers over heterogeneous terrain, Water Resour. Res. 42 (2006) 1–18, https://doi.org/10.1029/2005WR003989.
[25] R. Stoll, F. Porté-Agel, Large-eddy Simulation of the Stable Atmospheric Boundary Layer Using Dynamic Models with Different Averaging Schemes, Boundary-Layer Meteorology 126, 2008, pp. 1–28. URL: http://link.springer.com/article/10.1007/s10546-007-9207-4, 10.1007/s10546-007-9207-4.
[26] S. Basu, A. Lacser, A cautionary note on the use of monin–obukhov similarity theory in very high-resolution large-eddy simulations, Boundary-Layer Meteorol. 163 (2017) 351–355, https://doi.org/10.1007/s10546-016-0225-y.
[27] J.N. Friedman, R.T. Holden, Optimal gerrymandering: sometimes pack, but never crack, Am. Econ. Rev. 98 (2008) 113–144, https://doi.org/10.1257/aer.98.1.113.
[28] G. Cortina, M. Calaf, R.B. Cal, Distribution of mean kinetic energy around an isolated wind turbine and a characteristic wind turbine of a very large wind farm, Physical Review Fluids 1 (2016) 1–18, https://doi.org/10.1103/PhysRevFluids.1.074402.